DNS of a Mach 14 Flow Over a Sharp Cone in AEDC Tunnel 9

Ross Wagnild* , Shaun Harris† , Cory Stack‡ , and Bryan Morreale§
Sandia National Laboratories, Albuquerque, NM 87185, USA

A wind tunnel test from AEDC Tunnel 9 of hypersonic turbulent flow is analyzed using several fidelities of numerical simulation including Wall-Modeled Large Eddy Simulation (WMLES), Large Eddy Simulation (LES), and Direct Numerical Simulation (DNS). The DNS was forced to transition to turbulence using a broad spectrum of planar, slow acoustic waves based on the freestream spectrum measured in the tunnel. Results show the flow transitions in a reasonably natural process developing into turbulent flow. Several 2nd mode wave packets advect downstream and eventually break down into turbulence. The surface shear stress and heat flux agree well with a transitional RANS simulation. Comparisons of DNS data to experimental data show reasonable agreement with regard to mean surface quantities as well as amplitudes of boundary layer disturbances. The DNS does show early transition relative to the experimental data. Several interesting aspects of the DNS and other numerical simulations are discussed. The DNS data are also analyzed through several common methods such as cross-correlations and coherence of the fluctuating surface pressure.

Nomenclature

δ	=	Boundary layer thickness
k^T	=	Turbulent kinetic energy
M	=	Mach number
P	=	Pressure
q_i	=	Heat flux
q_i^T	=	Turbulent heat flux
R	=	Specific gas constant
T	=	Temperature
u_i	=	Velocity
u_τ	=	Friction velocity
γ	=	Ratio of specific heats
μ	=	Dynamic viscosity
ρ	=	Density
Re_τ	=	Friction Reynolds number
	=	
subscripts	=	
	=	
∞	=	Freestream quantity
e	=	Boundary layer edge quantity
$trans$	=	Property of transition
r	=	recovery quantity
w	=	Wall quantity

*Principle Member of Technical Staff, AIAA Associate Fellow
†Postdoctoral Researcher, AIAA Member
‡Senior Member of Technical Staff, AIAA Member
§Graduate Student and Intern, AIAA Member

I. Introduction

Turbulence models for hypersonic RANS simulations are notorious for having a large uncertainty in turbulent heat flux and shear stress, resulting in a large uncertainty for hypersonic vehicle designs. Such a large uncertainty leads to overdesigned thermal protection systems and less payload on flight vehicles. As a result of this large uncertainty, several efforts have begun working toward characterizing hypersonic turbulent boundary layers through experimental measurements or high-fidelity simulations, such as direct numerical simulation (DNS) or large-eddy simulation (LES) [1–11]. At Sandia National Laboratories, an effort has been started to look at high-fidelity simulation data for improving reduced order models in the areas of turbulent surface pressure fluctuations [12–14], turbulent heat flux, and aero-optical distortions in boundary layers [15]. Ideally, scientists would draw on a large array of turbulence data sources that vary Reynolds number, Mach number, wall temperature ratio, enthalpy, and other relevant quantities to build a solid foundation for improving hypersonic RANS turbulence models for use in applications such as random flight vibration loading and turbulent heat flux in flight. One of the goals of the current research is to build-out case data for model generation and evaluation. With trusted, high-fidelity simulation data, case data could be generated in regimes that are not achievable by the current set of ground test facilities or flight test vehicles. Before such high-fidelity simulation data can be used, validation efforts must be undertaken to build confidence in the simulation to provide an accurate description of hypersonic turbulence. Therefore, the current study seeks to extend the evaluation of the ability of the Sandia Parallel Aerodynamics and Reentry Code (SPARC) CFD solver [16] to simulate hypersonic turbulent flow over conical geometries. Previous work has shown reasonable success in modeling Mach 8 flow over a flat plate [7] and a cone in the Sandia HWT-8 tunnel [9]. The current work focuses on a sharp cone tested in AEDC Tunnel 9 using selected simulation data and comparing to data from the experiment. The methodology of the current work is similar to that of Huang et al. [9] and Liu et al. [11], with some exceptions: the full test article is simulated in one domain and an acoustic inflow of planar waves based on measured tunnel data is used for forcing transition. In addition to DNS, other high-fidelity simulations using LES and Wall-Modeled Large Eddy Simulation (WMLES) were performed with a turbulent inflow to better understand the DNS simulation results. The goal of the work is to establish credibility of the DNS and then explore various aspects of both the transitional and turbulent flow.

II. Simulation Setup

A. Flow Conditions and Geometry

As stated previously, the current work focuses on a wind tunnel experiment performed at AEDC Tunnel 9 and reported on in Marineau et al. [17]. The condition is called out as 'C1' in the paper and the freestream conditions are given in Table 1. The test article of this case was a sharp-nosed, 7-degree half-angle cone with a nosetip radius of 0.006 in or 0.152 mm. The cone was 1.550 meters long. The cone was instrumented with 53 PCB 132-A31 high-frequency pressure sensors, 20 Kulite XCS-093 high-frequency pressure sensors, 66 coaxial thermocouples, and 47 pressure taps for recording instability frequencies, heat flux, surface pressure, and boundary layer transition. In addition to the instrumentation on the cone, freestream pressure fluctuation data was taken with a pitot probe that contained a Kulite pressure sensor and a PCB132 pressure sensor. These data are used to match an acoustic inflow spectrum described below.

Table 1 Freestream conditions from the AEDC Tunnel 9 experiment.

Re (1/m)	M_∞	P_∞(Pa)	T_∞(K)	$\rho_\infty(kg/m^3)$	u_∞(m/s)	T_w(K)	T_w/T_r	T_w/T_e
12.1	14.4	263.1	45.7	1.94e-2	1974	296.11	0.18	2.57

B. Numerical Solvers

The numerical solver used for the DNS, LES (Large Eddy Simulation), and WMLES (Wall-Modeled Large Eddy Simulation) work is the SPARC CFD solver [16]. The code solves the 3-dimensional, compressible Navier-Stokes equations, both perfect and reacting gases, and contains several discretization and flux evaluation methods. For the current work, the cell-centered finite volume scheme was used to solve a perfect gas flow of N_2 over the test article. The inviscid fluxes were calculated with the 4th-order Kinetic-Energy-Conserving (KEC) scheme of Subbareddy and Candler [18] for the central scheme and the Modified Steger-Warming method to provide dissipation. A dissipation

switch from Larsson et al. [19] was used to minimize the application of dissipation through the solver domain. For the DNS, a minimum value of the dissipation switch was 0.15 due to the large gradients that form when turbulent eddies advect into the side buffer regions. The LES and the WMLES used a minimum value of the dissipation switch of 0.2. The LES was performed without a subgrid model (iLES). The wall model used for the WMLES was an equilibrium algebraic wall model. The viscous fluxes are 2nd-order and use gradients calculated using a weighted-least-squares fitting method. The time advancement scheme is a 2nd-order implicit method based on the point-Jacobi, backward difference formula. The viscosity for N_2 was calculated using Sutherland's Law with the form given in Eq. 1. The Prandtl number was 0.72 and the gas constant was 296.72307.

$$\mu(T) = 1.3993 * 10^{-6} \frac{T^{\frac{3}{2}}}{106.6667 + T} \tag{1}$$

The grid design simulations and the RANS computations used US3D[20, 21]. This code solves the compressible, reacting Navier-Stokes equations using a finite-volume approach and has several different inviscid flux schemes and time advancement methods. For this work, the inviscid fluxes were second-order accurate and were calculated using the Modified Steger-Warming method. The viscous fluxes were evaluated using gradient reconstruction calculated using the weighted, least-squares method. The time advancement was accomplished with the first-order, implicit DPLR method. US3D has several different turbulence models and the choice made for this study was the SA-Neg model [22]. As used in SPARC, a single-species, perfect gas of Nitrogen was used to simulate the tunnel flow. All properties were consistent with the exception of the viscosity model, which used the viscosity law described by Glowacki [23]. While the models are different, the differences are less than 2 percent over the range of temperatures in the problem.

The stability analysis for this study was computed using the STABL software suite[24]. The main component of the software suite used was PSE-Chem, which solves the reacting, two-dimensional or axisymmetric, linear parabolized stability equations (PSE) to predict the amplification of disturbances as they interact with the boundary layer. The base state for stability analysis was extracted from a quiet simulation on an axisymmetric warm-up mesh for the DNS. These data were converted for input into the PSE-Chem solver using the STABL user routines. Additionally, the properties of N_2 were matched to the SPARC simulations, including the viscosity law.

C. Grid Design

In order to properly design the mesh for the DNS, a transitional RANS simulation was performed with the transition location fit to match the data from Marineau et al. [17]. The transition model used in the RANS simulation is meant to mimic natural transition by modifying the effective viscosity in a manner similar to the evolution of turbulent intermittency observed in experiments and takes the form shown in Eq. 2. The output of the function, f, becomes a prefactor on the turbulent viscosity term in the momentum equation. The parameters used to specify transition in the problem were $x_{trans} = 0.369m$ and $\Delta_{trans} = 0.3527m$. Grid sizing parameters were extracted from simulation, two of which are shown in Figure 1. One objective of the current work was to target a value of Re_τ of 500, increasing from the previous similar study in Huang et al.[9]. Based on the sizing simulation, the necessary axial length should be approximately $0.8m$. The target grid spacing in the turbulent corridor of the mesh was $\Delta x^+ = 5$, $\Delta z^+ = 3.5$, $\Delta y_w^+ = 0.35$, and $\Delta y_e^+ = 1.0$, corresponding to approximately $62\mu m$, $40\mu m$, $4.5\mu m$, $13\mu m$, respectively. These scales were compared with and found similar to acoustic wavelength scales, targeting low dissipation on waves up to 800 kHz, enough to capture the primary and first harmonic frequencies that cause transition.

$$f(x) = \frac{1}{2}\left(\tanh\left[\frac{x - \left(x_{trans} + \frac{1}{2}\Delta_{trans}\right)}{0.2\Delta_{trans}}\right] + 1\right) \tag{2}$$

Based on these parameters, the DNS grid was created using the commercial software Pointwise and contains roughly 14.3e9 cells with 900 cells in the wall-normal direction, 1160 cells in the spanwise direction, and 13813 cells in the streamwise direction. The grid is evenly spaced in the spanwise direction near the nose in the receptivity region and clusters cells to a focused corridor to capture linear and nonlinear transition mechanics shown in Figure 2. The refined corridor continues past transition to the turbulence region. The grid contains a volume of half of the cone with coarse buffer regions around the high-resolution corridors as well as at the outlet to minimize wave reflection. The high-resolution corridors span 22 degrees which is approximately 6.25 boundary layer thicknesses at the end of the turbulence corridor. The refined mesh has an axial extent of $0.80m$, as discussed above, with a outlet buffer region

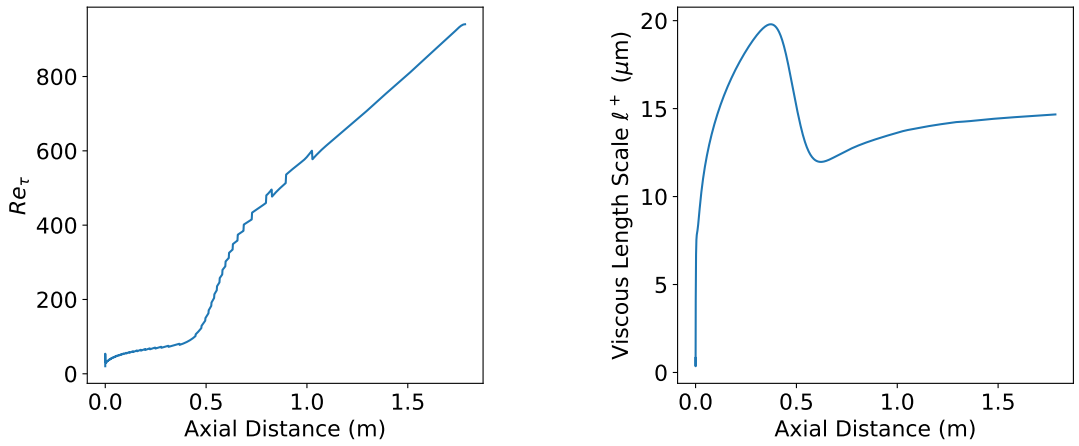

Fig. 1 Grid sizing parameters from the transitional RANS simulation. The friction Reynolds number is shown on the left and the viscous length scale is shown on the right.

extending to 1.2. Part of the reason for the length of this buffer was to reduce time to remesh the volume when extending the turbulent corridor.

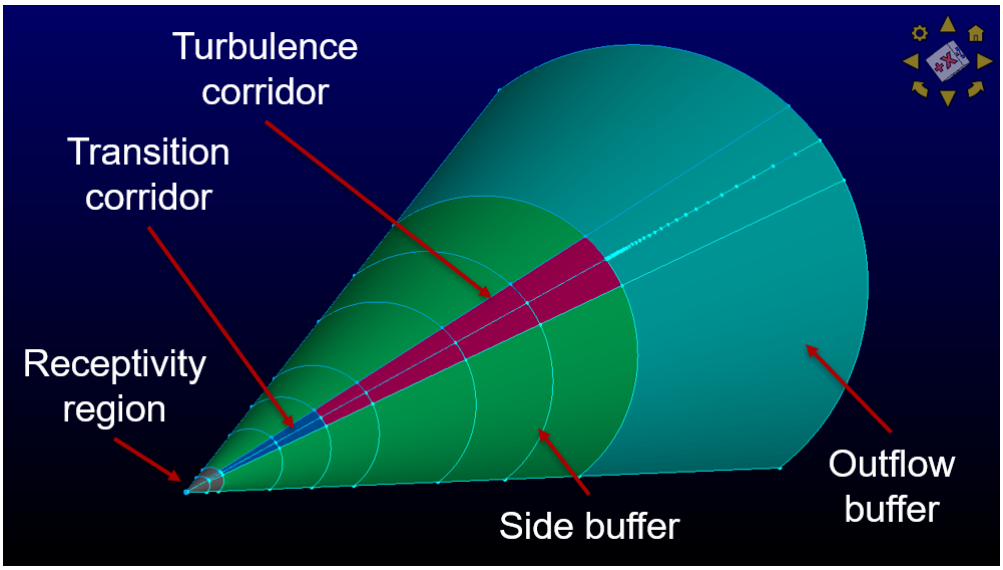

Fig. 2 Surface grid topology for the DNS. The grid comprises 5 sections: a high-resolution nosetip region for receptivity (maroon), a transition corridor (blue), a turbulence corridor (red), a buffer region (green), and an outlet buffer region (teal).

D. Freestream Acoustic Forcing

A freestream forcing of planar acoustic waves was used to cause transition to turbulence on the cone in a manner similar to that of the experiment. This process was modeled after that described by Balakumar and Chou [25], using a discretization of the measured freestream amplitude of 1 kHz, ranging from 6 kHz up to 800 kHz, plotted in Figure 3a against the wind tunnel noise measurement. A random phase angle in the wall-normal direction ranging from 0 to 25 degrees, shown in Figure 3b, and a random phase shift ranging from 0 to 180 degrees was specified for each frequency simulated. This is different from the spanwise phase angle used in Huang et al. [9]. Previous work has shown non-zero

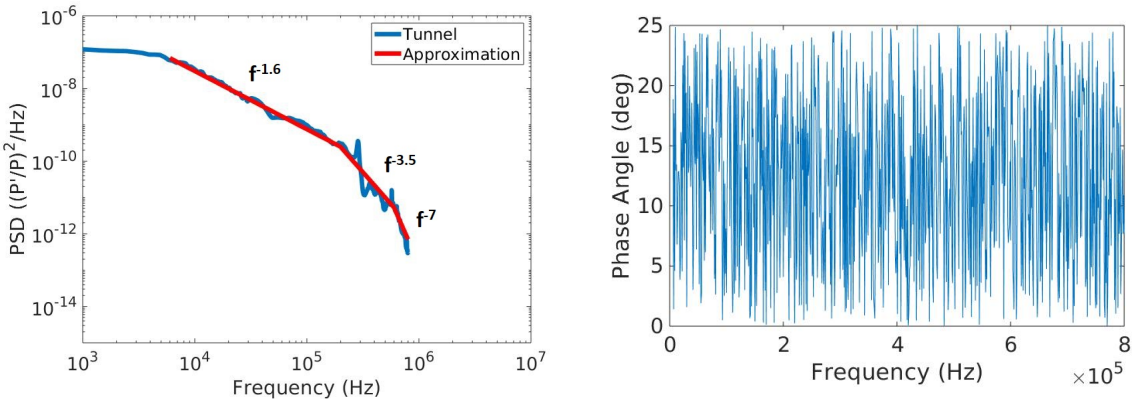

(a) PSD approximation

(b) Phase angle

Fig. 3 The PSD approximation of the tunnel noise spectrum (a) and the phase angle assigned to each frequency for the numerical noise environment (b).

phase angle obtains a more realistic nonlinear transition process. The formula given in Chaudry and Candler [26] was used to convert the post-shock measured pitot amplitude to a pre-shock freestream amplitude for slow acoustic waves.

$$\chi_{p,p_0} = \left(\frac{M_\infty^2 - 2M_\infty + \frac{1}{M_\infty}}{\gamma M_\infty^2 - \frac{\gamma-1}{2}} \right)^2 \tag{3}$$

E. LES and WMLES Method

For both the LES and WMLES, a precursor, fully-turbulent RANS simulation was run to generate the necessary input data to seed the inflow plane at x=0.45m with a synthetic turbulent boundary layer generated by the synthetic digital filtering method of Adler [27]. This inflow plane location was informed by estimating the location from the experiment that reaches turbulent flow. In terms of the incoming boundary layer thickness (δ_0), the length of this development region corresponds to $20\delta_0$, which has shown from experience to be sufficient for quantities of interest for flow conditions of this work. The RANS simulation was utilized to generate the grid densities required for the subsequent LES and WMLES cases. Using the RANS flow state on the LES inflow plane as a reference, the LES grid resolution was specified to $\Delta x+ = 10$, $\Delta y+ \ 0.07$, and $\Delta z+ = 5$, with 201 nodes placed in the wall-normal direction within the boundary layer region, and uniform spacing in the streamwise and azimuthal directions. Meanwhile, the WMLES grid density was chosen based on the incoming boundary layer thickness from the RANS solution, where we utilized a uniform spacing of 20 nodes per δ_0 are specified in the streamwise and azimuthal directions, and 51 uniformly spaced nodes in the wall-normal direction within the boundary layer region. Due to the larger computational cost of the LES, the LES was performed on a smaller streamwise subdomain than the WMLES, although both simulations utilized a 20 degree azimuthal sector. Specifically, the LES was performed from $0.45m < x < 1m$, while the WMLES was performed over $0.45m < x < 1.77m$. These grid densities combined with the spatial extent of the domains resulted in grids containing 2671x269x303=211e6 and 5745x119x101=67e6 nodes for the LES and WMLES respectively.

F. Computing Architecture

The Lawerence Livermore National Laboratory Sierra HPC was used to perform the DNS computation described in the current study. Sierra comprises 4320 nodes with 4 GPUs and 44 CPUs each. Several submissions of 2000 nodes using 8000 GPUs allowed for a relatively short computational time given the size of the simulation. The SPARC solver is built on Kokkos to take efficient advantage of the CPU/GPU architecture.

III. Results

A. DNS Simulation Overview

Currently, 1.31 milliseconds of simulation time has been computed, with averaging over 0.548 milliseconds of the total simulations time, approximately 1.45 flow times. A sample view of the surface pressure contours, shown in Figure 4, shows the full evolution of the disturbance field over the cone. Near the nose of the cone, planar boundary layer fluctuations amplify according to the resonant frequency of the boundary layer. At approximately $0.25m$, the planar waves develop small azimuthal perturbations that grow rapidly, but maintain order. By $0.35m$, the azimuthal variations begin to break symmetry and form local areas of chaotic flow. These could be due to the variation in amplitudes of different frequencies interacting in the non-linear breakdown portion of the transitional boundary layer. Roughly 4 spots can be seen in the image with less chaotic flow in between. The last spot, centered at approximately $0.54m$, has nearly merged with the remainder of the turbulent boundary layer flow starting at $0.6m$. Because each side buffer region coarsens only in the spanwise direction, these regions are only capable of maintaining the primary transition frequency in the range of 200-400 kHz.

Based on the surface pressure contours there are a couple interesting aspects to note. First, there exist elliptical shapes, centered at $0.18m$ in Figure 4, among the predominantly stream-wise-aligned wave fronts. This is thought to occur because of the wave front inclination against the cone frustrum should form a parabola profile as opposed to a circular profile for a plane aligned with a cone axis. The spots of chaotic flow develop primarily around these elliptical variations. Second, while there is no symmetry enforced in the transitional region between $0.2m$ and $0.3m$, the surface pressure contours show a symmetric structure advecting down the cone. The cause of this is thought to be the constant phase angle of each of the frequencies forced in the freestream. The symmetry of the simulation is only broken when the boundary layer fluctuations become sufficiently strong. Given a more realistic forcing function, such as that used in [11], it is expected that the spots of chaotic flow would lack symmetry.

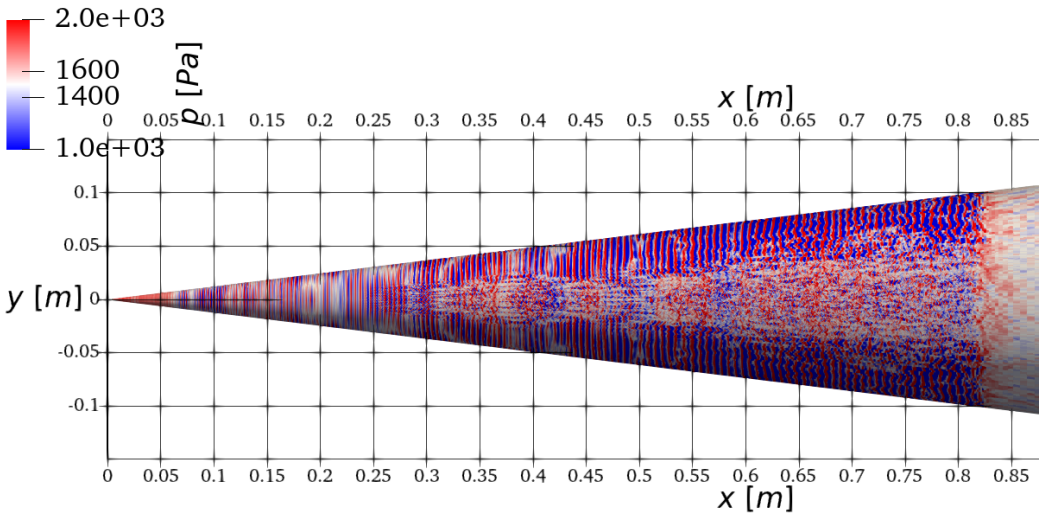

Fig. 4 Wall pressure contours with the colorbar scale clipped to show the disturbances qualitative behavior.

An instantaneous view of the density field, shown in Figure 5, conveys the flow structures that cause the surface field in Figure 4. Radiation from second mode waves are visible at the left side of this, while broadband radiation is visible from the turbulence on the right. Also note the shock wave bending due to low-frequency, high-amplitude waves from the inflow. As with the surface pressure, the effect of the coarse resolution in the side buffers is to eliminate turbulent fluctuations and prevent reflections off the boundaries of the domain, shown down the length of the middle of the plot.

B. Surface Mean Properties

One of the primary goals of the work is to evaluate the accuracy of the turbulence models used in the RANS simulations. This accuracy is evaluated based on surface pressure, heat flux, and shear stress, shown in Figure 6. To compute each of these mean properties from the DNS, data was first span-averaged to the centerline and saved off. Time

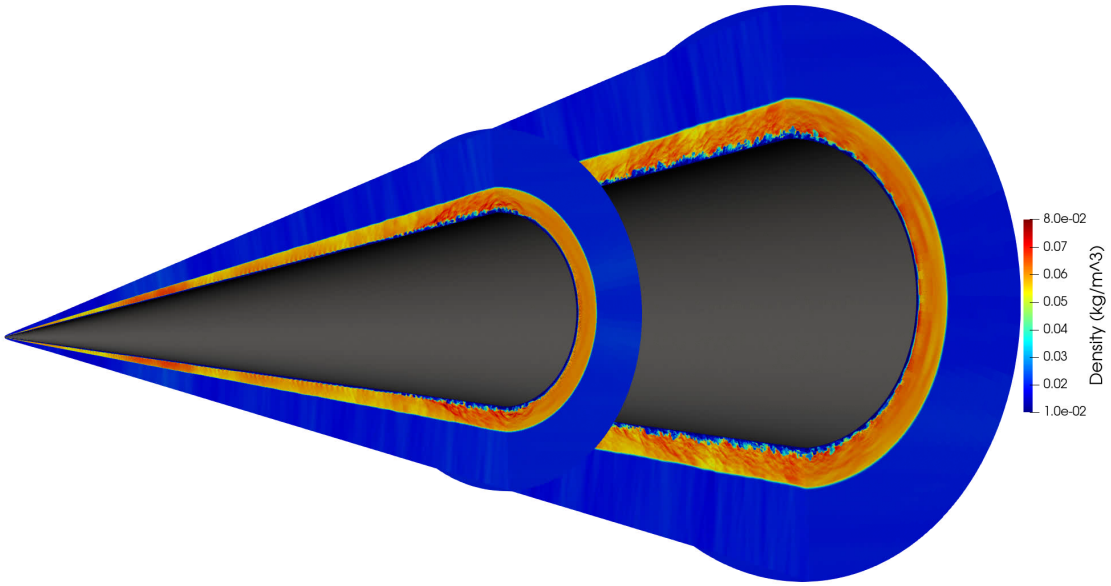

Fig. 5 Flowfield density contours on two axial slices and a slice through the middle of the domain. The flowfield has been mirrored to complete the view of the cone.

averages of each quantity were taken across the full length of the averaging window, but also from each submission to the Sierra cluster to understand the level of variation between submissions. In each plot, the legend entry 'Averages' indicates all of the averages from each submission whereas the dark blue 'DNS Average' indicates the average over the full averaging window. The transitional RANS simulation was evaluated to best match the slope of transitional heat flux of the DNS and has parameter values of $x_{trans} = 0.269m$ and $\Delta_{trans} = 0.39m$.

Focusing first on the surface pressure in Figure 6a, the DNS smoothly transitions between the fully-laminar and fully-turbulent RANS simulations. The transitional RANS shows an overshoot in pressure which is not observed in the DNS. The LES and WMLES both take until approximately $0.6m$ to accommodate the pressure from the inlet condition. The transitional RANS shows the best agreement with the LES and WMLES downstream of the DNS outflow boundary, however the fully-turbulent RANS is relatively close (approximately 1 percent).

Focusing next on the heat flux, shown in Figure 6b, the data show excellent agreement in the laminar region between DNS and the laminar Navier-Stokes simulation, as expected. This indicates that the amplitude of the boundary layer fluctuations are not of sufficient amplitude to distort the viscous properties of the boundary layer. The DNS does show unexpected behavior at the first departure from laminar heating. The transition RANS demonstrates the commonly observed behavior for heat flux during boundary layer transition. It is currently unknown what causes the odd behavior in the DNS simulation, however the disturbances have reached sufficient amplitude to distort the mean boundary layer profile without resulting in transition. This is attributed to the forcing acoustic environment of the simulation. Despite this odd behavior, a more natural behavior occurs where the DNS and transitional RANS profiles meet at approximately $0.37m$. Interestingly, the transitional RANS is nearly identical to the DNS through peak heat and down on the turbulent side of the curve. Unfortunately, the DNS domain is not of sufficient length to know if the turbulent heat flux would asymptote to the fully-turbulent RANS simulation. However, based on the transitional RANS behavior, it is assumed that the DNS captures only the overshoot portion of the turbulent heat flux and that it would evolve to nearly match the fully-turbulent RANS just as the transition RANS does. This is notably different than the LES simulation, which, after its accommodation length of approximately $0.2m$, follows the curve of the fully-turbulent RANS simulations. This is not true for the WMLES, which is expected and part of the motivation for improving WMLES models to better capture turbulent heating. The inflow of the LES and WMLES targets an equilibrium turbulence, whereas the transitional nature of the DNS may not have reached equilibrium turbulence. Based on the numerical comparisons alone, the RANS model, in this case the SA-Neg model, does very well capturing the behavior of the higher fidelity simulations. The last observation to make on the DNS average concerns the sharp drop-off at the end of the data, which is due to the drop in grid resolution into the buffer region.

Lastly, the shear stress has similar behavior as the heat flux due to the viscous nature of both quantities. The only

additional observation to make regarding the shear stress is that the transitional RANS and the LES agree better with the fully-turbulent RANS simulation, once each has completely adjusted the boundary layer to fully-turbulent flow.

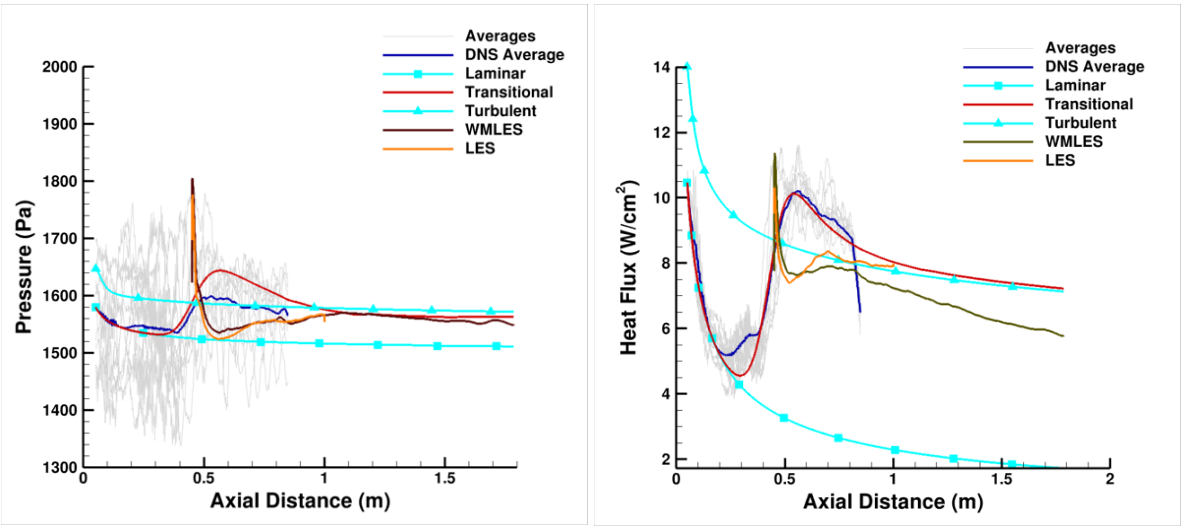

(a) Mean surface pressure **(b) Mean heat flux**

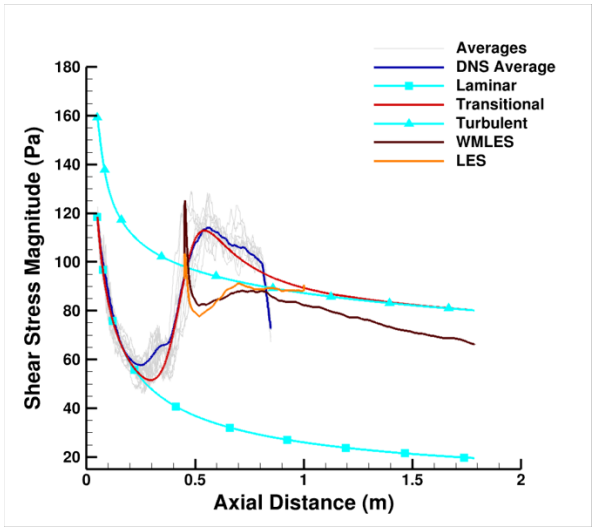

(c) Mean shear stress magnitude

Fig. 6 Data for mean properties of surface pressure (a), heat flux (b), and shear stress (c) computed from the DNS, LES, WMLES, and RANS.

C. Surface Statistical Behavior

Utilizing common signal processing functions, further insights into the data can be gained. The temporal autocorrelation, 7a, begins with strong periodic behavior, indicating the repetitive waves of second mode disturbances. This periodic behavior degrades as the axial location approaches the non-linear breakdown stage of transition (approximately $0.34m$) and takes on a chaotic nature in the turbulent region ($0.65m$ and $0.77m$). An interesting insight gained from this analysis lies in the fluctuating amplitude over longer time periods. At a given axial location, it is assumed that a single frequency maintains dominance due to the behavior of second mode instabilities, although in practice this probably shifts over a relatively small range. Under this assumption, the amplitude of the temporal correlation would be a cosine function with fixed envelope given the constant amplitude of each frequency on the inflow boundary condition. However, the temporal correlation shows a variable envelope over time delay, suggesting that the

growth of the second mode disturbances is being modulated by other frequencies in the acoustic forcing environment. Normally, a linear assumption is made on the initial growth of disturbances in the boundary layer. However, as evidence in Figure 5, some low frequency waves have sufficient amplitude to bend the bow shock and the boundary layer.

The streamwise autocorrelation function, Figure 7b shows a similar story, although with this function, it is easier to observe the variation of frequency down the length of the laminar portion of the boundary layer. From $0.1m$ to $0.3m$, the first peak of positive spatial correlation moves to greater distances, indicating that the wavelength of the dominant component of the signal is getting longer downstream. The regularity of the correlation function begins to breakdown at $0.4m$ and is mostly gone by $0.5m$ indicating the transition to chaotic flow leading to turbulence downstream, which is maintained until the end of the refined region.

The spanwise autocorrelation function, Figure 7c, elaborates on the beginning of the spanwise symmetry breakdown. The fluctuations are nearly identical in the spanwise direction at $0.1m$ and $0.2m$, reflective of the two dimensional nature of the disturbances at these locations. By $0.3m$, the spanwise correlation has degraded further from the small beginnings at $0.2m$, indicating the noticable breakdown in wavefronts observed in Figure 4. Symmetry in the correlation function breaks down by $0.4m$ and is fully turbulent by $0.6m$, consistent with the other correlation functions.

As with previous work [7, 9, 14], the streamwise and spanwise coherence data is important for the validation of reduced order models used in applied analysis. The common functional form with which to compare is from Corcos [28] and is shown in Eq. 4. The spanwise and streamwise coherence data were computed and compared to the Corcos relation for the laminar and turbulent regions of the flow u, shown in Figure 8. The laminar region of the flow shows a high coherence in both directions due to the periodic behavior during the modal growth prior to transition. The turbulent region shows promising results for normalized frequencies below 5. Above 5, the data show a higher level of coherence than previous of studies [7, 9], the cause of which is currently unknown. More spatial evaluations of coherence and further investigation into the flow will elucidate the cause for this behavior.

$$\Gamma\left(\Delta x, \Delta y, \omega\right) = e^{-\alpha_1 \omega |\Delta x|/U_c} e^{-\alpha_2 \omega |\Delta y|/U_c} e^{i\omega \Delta x/U_c} \tag{4}$$

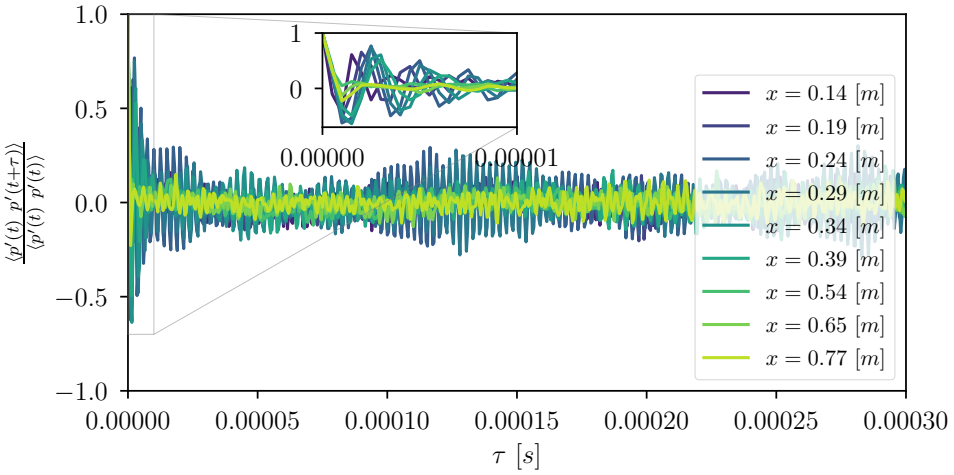

(a) Temporal autocorrelation of the pressure fluctuation.

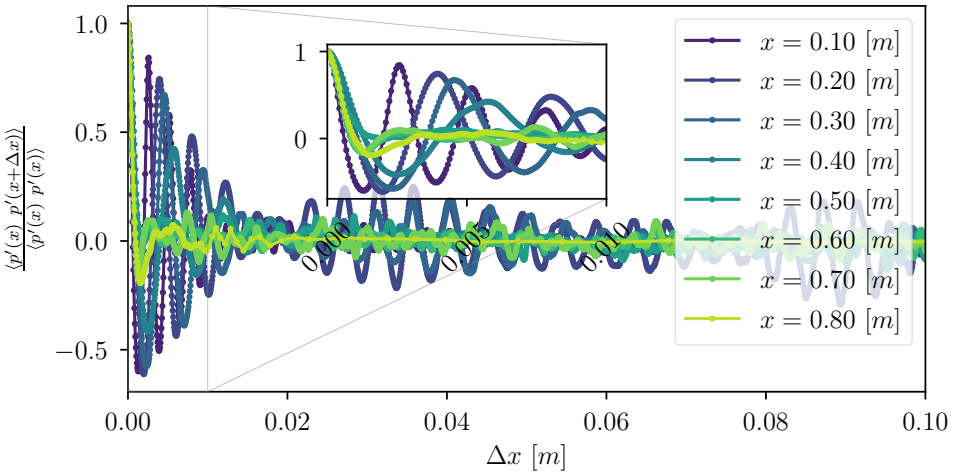

(b) Streamwise autocorrelation of the pressure fluctuation.

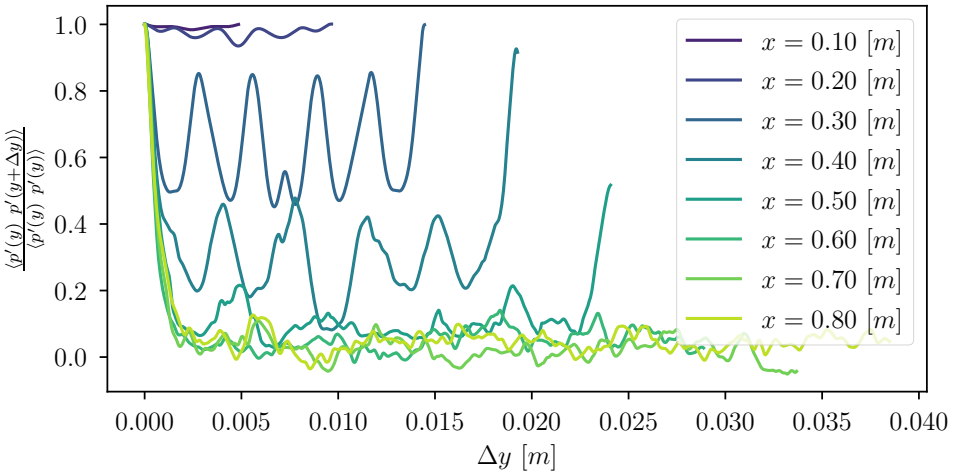

(c) Spanwise autocorrelation of the pressure fluctuation.

Fig. 7 Autocorrelation using the wall pressure fluctuation at various locations. Periodic correlations can be found early on in the laminar region $x < 0.4\ [m]$, followed by nonlinear breakdown and eventual collapse to turbulent correlations $x > 0.6\ [m]$.

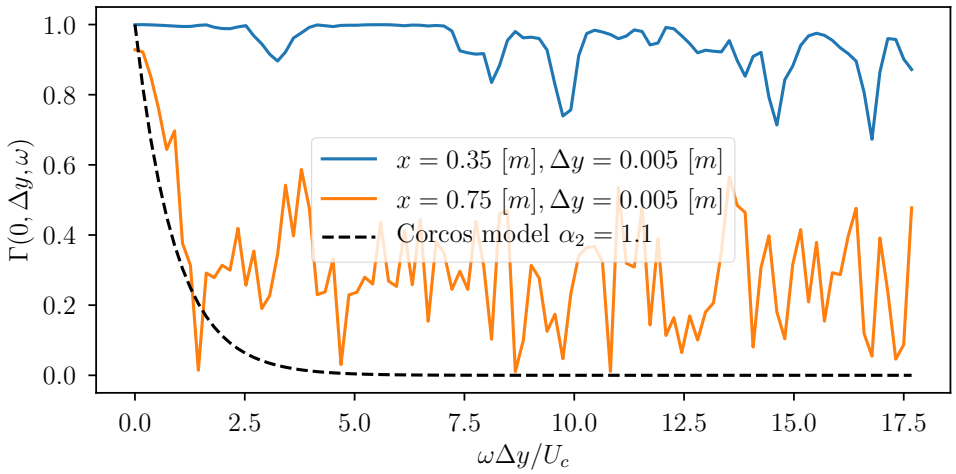

(a) Spanwise separated coherence.

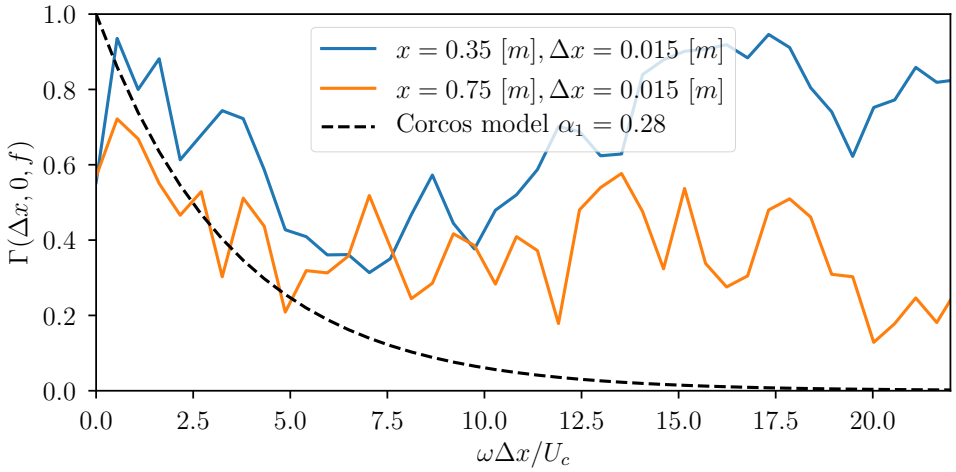

(b) Streamwise separated coherence.

Fig. 8 The coherence is evaluated and compared to the typical Corcos model for a laminar and turbulent region. The turbulent region shows some promising results for normalized frequency below 5 when compared to the Corcos model, but seems to show higher than typical values for higher frequencies. The laminar region is high for all frequencies of interest due to the periodic behavior and modal growth region prior to transition.

IV. Comparison with Experimental Data

As stated in Section II.A, the experimental test article had both mean data sensors and high-frequency pressure sensors. Ideally, the DNS would match both mean and high-frequency data, given the small number of computational models involved in the simulation. As inferred from the simulation setup and results, there are different transition locations required of the transitional RANS to match the experiment and the DNS. Comparing the numerical data against the experimental data, shown in Figure 9, the numerical approaches achieve less than ideal agreement with the experiment. The most notable difference is the that of the transition location: the tunnel shows a departure from laminar heating in the vicinity of $0.35m$, while the DNS departs laminar heating at $0.2m$ and doesn't engage transition until $0.3m$. Because of this, it is difficult to compare turbulent heating levels beyond the asymptotic value of the fully-turbulent RANS simulation. An alternative option would be to run the transitional RANS to approximately match the experimental transition location. A reasonable fit to the slope of transition heating occurs for $x_{trans} = 0.348m$ and $\Delta_{trans} = 0.55m$, shown in Figure 10. This comparison assumes that the transitional RANS is reasonably capturing the flow in the tunnel, which likely may not be true despite the earlier agreement between the DNS and the transitional RANS. Given this assumption holding, The error in heat flux between the RANS and the tunnel data varies from 6 to 15 percent. The same error would be true of the fully-turbulent RANS simulation assuming the last few gauges on the cone have settled to an asymtotic trend after an overshoot in heat flux.

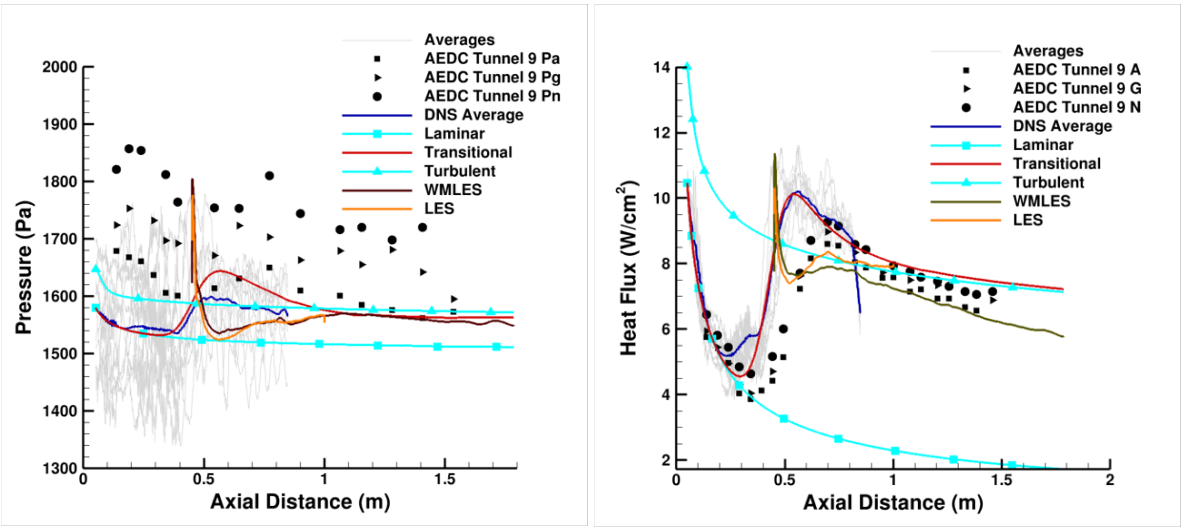

(a) Mean surface pressure **(b) Mean heat flux**

Fig. 9 Data for mean properties of surface pressure (a) and heat flux (b) comparing computations to experimental data.

The high-frequency data shows slightly better agreement than mean quantities, considering the obvious mismatch in transition location, shown in Figure 11. At each sensor on the cone, a similar data extraction was performed from the DNS surface field. The surface was sampled at 2 MHz. At each sample time, pressure on the faces that compose the working area of a PCB132 sensor was averaged and recorded. These data were used to compute the PSD at each station. These data show a similar story to all of the previous discussion. The first three plots show very good agreement with the amplitude of the measure data as well as the peak and width of amplified disturbances. At $0.24m$, the DNS shows a definite harmonic peak from the primary frequency, which continues to strengthen at $0.29m$ and $0.34m$. By $0.39m$, the primary frequency band amplitude has begun to decrease due to non-linear interaction spreading power to surrounding frequencies. Meanwhile, the experiment doesn't start to show a harmonic peak until $0.29m$ and a peak in primary frequency growth at $0.39m$. By $0.54m$, the DNS has completed saturated to broadband noise and lost its second mode peak. By $0.77m$, the experiment also shows a turbulent spectrum and the two have similar amplitudes, with the exception being the low frequency band, where the DNS has insufficient time sampling to evaluate.

The early agreement of amplitude across the frequency space to the experiment shows that the forcing acoustic environment is relatively close to the tunnel, at least on a log scale. The head-on, planar wave assumption of the acoustic forcing may be too direct and result in higher-amplitude disturbances in the boundary layer leading to early transition, despite any potential numerical dissipation. A more representative boundary condition, such as that generated by Liu et

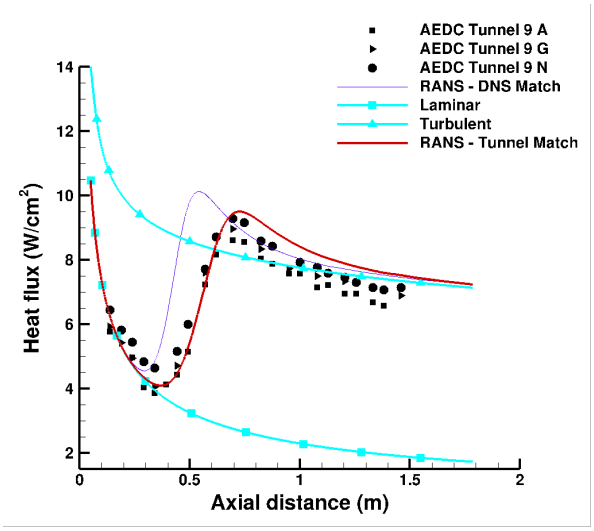

Fig. 10 Heat flux comparison of tunnel-transition-matched RANS to tunnel data.

al. [11], is thought to be necessary to improve the agreement with tunnel transition. Based on the transitional RANS, however, this would likely not improve agreement with the turbulent heat flux.

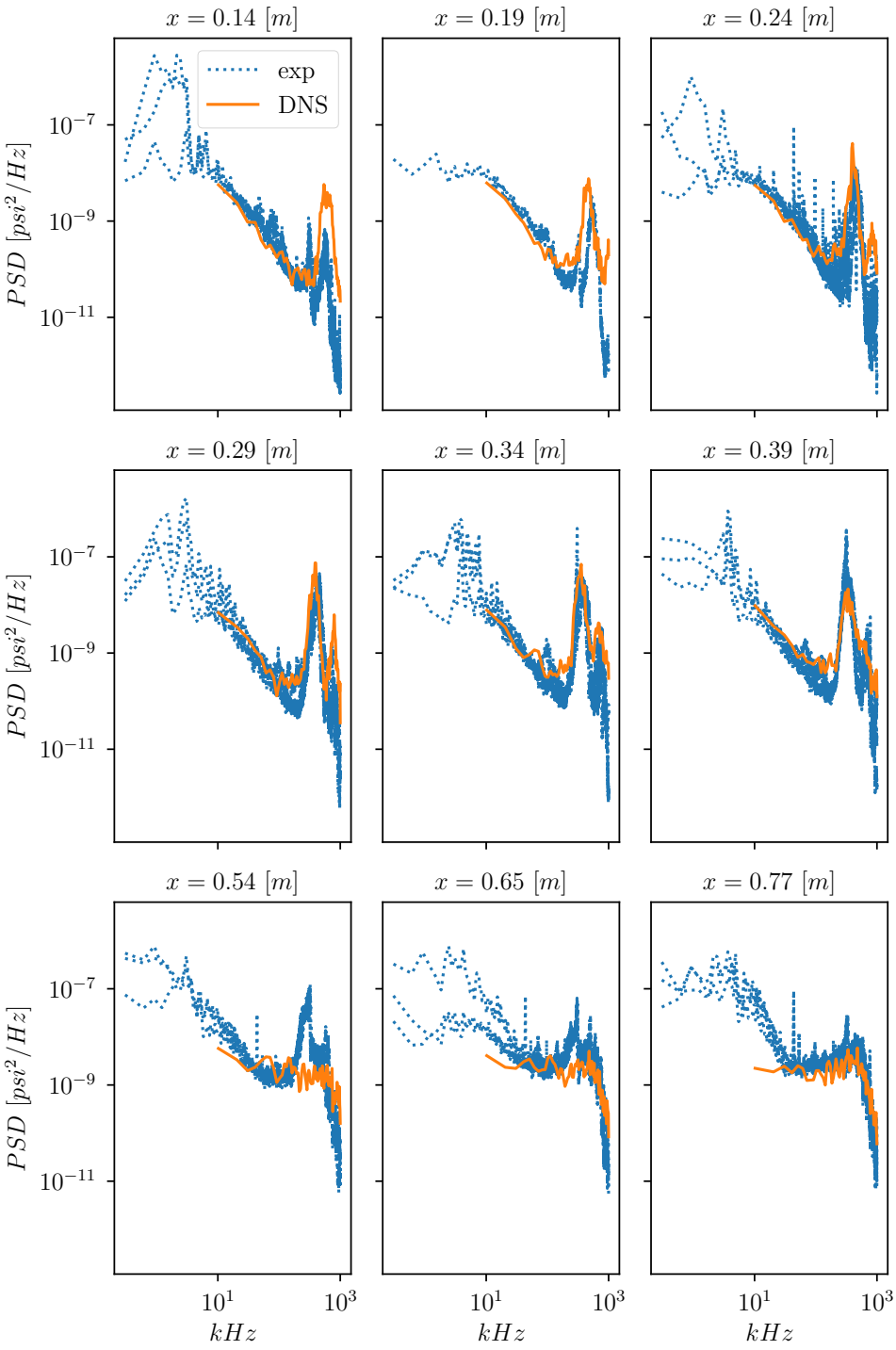

Fig. 11 Comparison of the wind tunnel pressure measurement PSD vs the related simulation. Excellent agreement is observed early on in the transition process for the peak frequencies of interest. It is shown here that the simulation seems to transition sooner and yields fairly broadband frequency around the $x = 0.54$ $[m]$ where the experiment is still showing significant modal interaction during the transition process.

A. Turbulence Discussion

As the flow naturally transitions from laminar to turbulent flow there is a characteristic peak in heating and skin friction. After this post transition peak the values settle to turbulent trends that are representative of fully developed equilibrium turbulence. Fully developed turbulence is essentially established when the flow has lost all memory of its transitional path and non-dimensionalized flow values are no longer a function of streamwise location [29] . More rigorously, mean production and dissipation rates approximately balance each other in the log layer for boundary layers in turbulent equilibrium. To rigorously establish the state of the turbulent boundary layer, energy budgets are needed to confirm the most stringent definition of equilibrium turbulence. In lieu of energy budgets, useful inference may be taken from figure 6 which shows the mean surface properties of the DNS against experiment. It is seen that mean DNS heating nicely tracks the experiment up to the $x = 0.8m$ streamwise station where the DNS domain ends. At the end of DNS domain, the experiment is still in its overshoot phase and relaxing. These findings point to the likely fact that even at $x = 0.8m$ the DNS is experiencing transitional turbulence and does not meet the criteria to constitute being label an equilibrium turbulent boundary layer.

Complicating matters is the pressure measurement PSD comparisons seen in figure 11. Looking at the x=0.77m axial station it appears as if the transitional spectral humps have been completely washed out into a broad band turbulent spectra where there is good agreement between DNS and experimental profiles. This last pressure spectra give the impression that the flow has developed into a mature turbulent boundary layer. The coherence data seen in figure 8 adds some much needed context. At $x = 0.75m$, in both the streamwise and spanwise calculations, there appears to be a significantly non-zero coherence. Calculations from Huang et al. [9] on a Mach 8 equilibrium turbulent boundary for a similar geometry layer show significantly smaller surface pressure coherence. This indicates that there might be residual "memory" of the transition being seen in the turbulence. The mean heating trends, pressure PSDs, and coherence calculations seem to hint toward the conclusion that the state of the boundary layer at $x = 0.8m$ is indeed turbulent, but not quite in turbulent equilibrium yet.

The experimental heating seems to indicate that a domain nearing 1.5 meters might be needed to capture the equilibrium turbulent boundary layer. The increased domain in the streamwise direction increases both the grid count and length of flow through times, which non-linearly increases the computational cost. To more efficiently directly simulate the near equilibrium turbulence seen in the experiment a new DNS is underway. The current work emphasizes direct numerical simulation of laminar to turbulent transition, and the upcoming work will specialize in efficiently capturing turbulent physics. As turbulent statistics are incredibly difficult to obtain experimentally the future calculations will analyze these statistics along with many of the metrics discussed in the current work. Analyzing these statistics will allow for analysis of turbulent Prandtl numbers, the validity of Boussinesq based theory, and the effects of extremely cold walls on a modestly turbulent equilibrium boundary layer.

V. Comparison with Stability Analysis

Part of the ongoing work related to this DNS lies in verifying the growth of various frequencies numerically as well as evaluating the effects of any numerical dissipation. To do this, the DNS is first compared directly to stability analysis. As stated previously, the down-sampled base state from an axisymmetric grid with identical streamwise and wall-normal spacing was used to compute the stability analysis. The stability diagram on the left, Figure 12a, outlines the frequencies of interest for the second mode. Additionally, a small band at higher frequency is observed indicating that some third mode can have some nonzero growth within the range of the frequencies studied in this work. The right figure shows the associated growth using the N factor for streamwise location. Two frequencies, $800kHz$ and $300kHz$, are highlighted for later comparison. Comparing this N factor envelope to the DNS and Tunnel transition locations shows a transition N factor of 4.3 and 4.9, respectively. Further work will characterize the breakdown amplitude for comparison to Marineau et al. [17].

Based on the root-mean-square (RMS) of pressure fluctuations, p'_{rms}, an N factor can be calculated from the DNS data using $N = \log(p'_{rms}(x)/p'_{rms}(x = x_{min}))$, where x_{min} is the streamwise location with the lowest wall pressure disturbance magnitude. The maximum of this calculated N factor from the DNS has a value of approximately 2.2, which differs from the linear estimate calculated from STABL, shown in Figure 13. This is not unexpected given the level of non-linear action evidence in the surface contours and PSD plots shown in previous sections. The DNS data also show two peaks in disturbance growth along the cone: one at $0.1m$ and one at $0.34m$. This second peak is an expected part of transition, however, the first peak requires more investigation. Evaluating the RMS of the Fourier Transform at $300kHz$ and $800kHz$, Figure 14, shows that the first peak is due to high-frequency disturbance amplification greater than that predicted by the linear analysis of STABL, Figure 12b.

In order to evaluate the behavior of the SPARC solver during the linear growth phase of the boundary layer and hopefully identify the root cause of the first peak, individual frequencies of acoustic waves are simulated on the same mesh that provided the base state for stability analysis. The amplitude of the waves is smaller than the main DNS in order to maintain linear growth and decay for comparison to the linear stability analysis. Although, these simulations haven't completed converging, the N factor behavior is consistent with the stability analysis, shown in Figure 15, although the acoustic simulations reach a higher-than-predicted N factor.

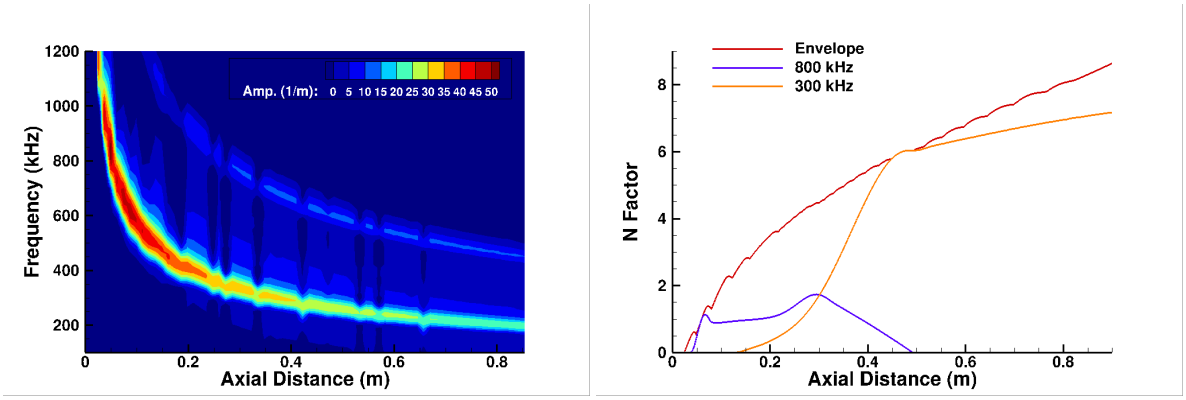

(a) Stability diagram **(b) N factor envelope**

Fig. 12 Stability diagram and N factor envelope computed using STABL for the current conditions. Two frequencies, 800 and 300 kHz, are called out for comparison to acoustic simulation.

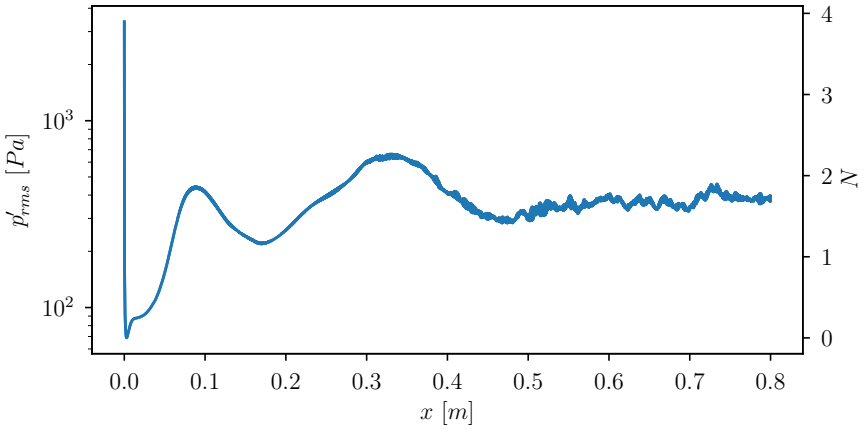

Fig. 13 Plot of pressure RMS and N factor growth using the wall values prior to full breakdown to turbulence. The N factor is calculated from p'_{rms}, thus the same line corresponds to the log scale on the left vertical axis for the RMS of wall pressure and the same line correponds to the right linear scale vertical axis for the associated N factor.

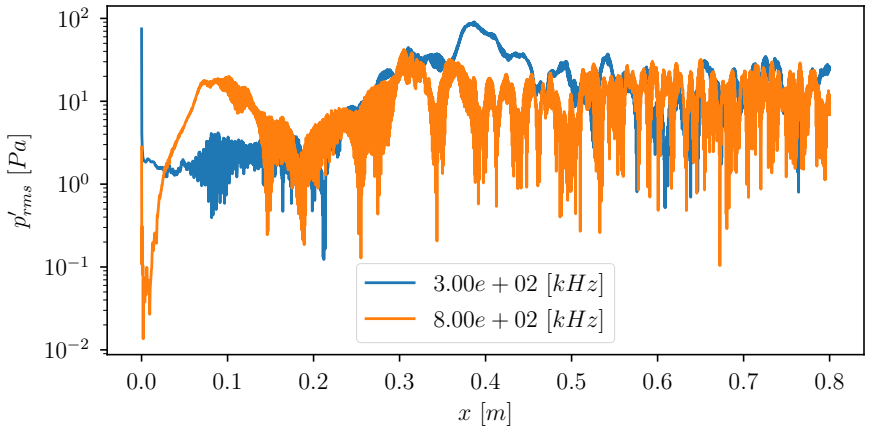

Fig. 14 RMS of the Fourier Transform of the wall pressure along the wall corresponding to 300 kHz **and** 800 kHz**. The higher frequency has two peaks corresponding to the two regions of growth observed in the stability diagram corresponding to that frequency. The lower frequency has just one main growth region.**

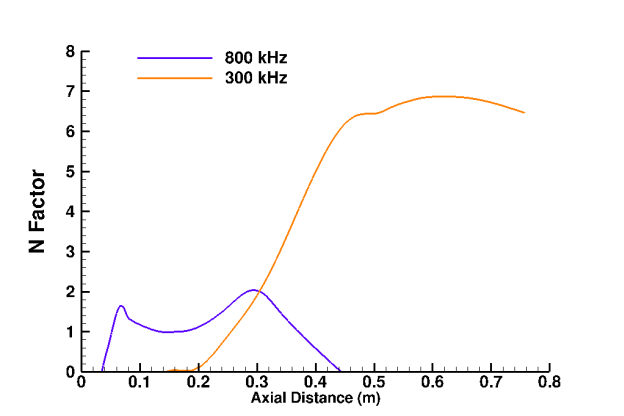

Fig. 15 N **Factor calculated from the individual acoustic simulations for** $300kHz$ **and** $800kHz$**.**

Isolating the N factors versus frequency at select locations allow for a qualitative comparison to the PSD's calculated from the DNS data. The N factors calculated from STABL are shown at every $0.1m$ along the cone until the boundary layer reaches turbulence, Figure 16. The natural progression from high frequency disturbances to lower frequency disturbances occurs as the boundary layer thickens. Comparing the STABL computations to the PSD's extracted as similar locations, Figure 17, shows nearly identical peak frequencies. The higher amplitude PSD peak shows at $0.1m$ followed by a lower amplitude peak at $0.2m$ is not expected, although it is consistent with the behavior show in Figure 13. By $0.3m$, the PSD shows a strong harmonic peak centered around $800kHz$, explaining the large growth of the that frequency in Figure 14. At $0.4m$ there remains a small portion of the primary disturbance peak centered near $350kHz$ before the PSD's flatten into a turbulent spectrum.

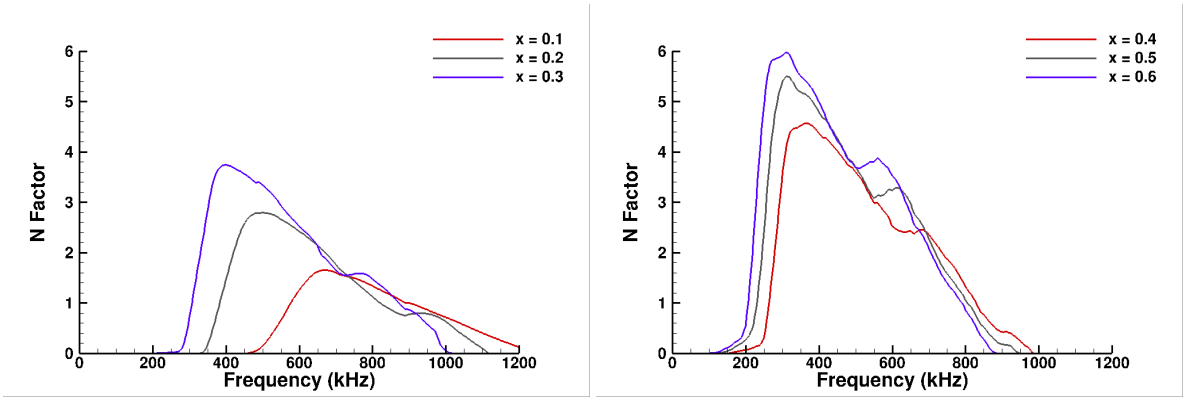

(a) N Factors at $x <= 0.3m$ **(b) N Factors at** $x > 0.3m$

Fig. 16 N factor versus frequency plotted for several different locations on the cone.

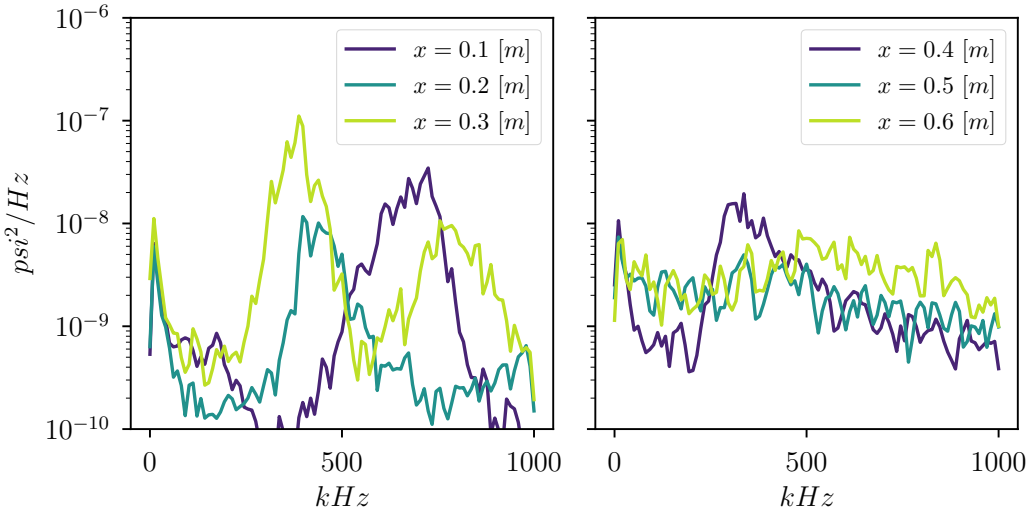

Fig. 17 PSD of DNS along centerline at various streamwise locations covering the laminar, transitional, and turbulent regions.

VI. Conclusions and Future Work

The process and initial analysis of a Direct Numerical Simulation of Mach 14 flow over a sharp cone was presented. The analysis shows many interesting features present with regard to boundary layer transition, turbulent heating, and high-frequency disturbance content. Overall, the simulation agrees well with the experimental data from AEDC Tunnel 9. Reasonable agreement is also found for comparisons with linear stability theory in terms of amplified frequency content.

While several interesting aspects of the high-fidelity simulations performed in this work were discussed, there are many questions that need to be investigated to better understand both the transitional and turbulent physics. In order to have confidence in the simulation results, it is necessary to understand the cause for the departure from laminar heating prior to boundary layer transition. Also, the two peaks in surface pressure RMS were not expected and a cause needs to be determined. Understanding the aspects of the acoustic forcing that result in early transition relative to the experiment would be important for future improvements. Lastly, further understanding the nature of the turbulence captured in the DNS will help determine its relevance for use in model generation. If the boundary layer flow is a transitional turbulence, then it training reduced order models to the elevated heat flux would not suite a generic hypersonic turbulence model.

Future work for this problem involves further investigation into the effects of numerical dissipation on the simulation and pursuing explanations for the various phenomena discussed in this paper. Additionally, future publications will focus on the physics associated with the equilibrium turbulence observed in the experiment.

Acknowledgements

The authors thank George Moraru and AEDC Tunnel 9 for sharing data from the experiments. They also thank Neal Bitter for helping to lay the foundation of the high-fidelity simulation capability at Sandia. The authors also thank Prof. Lian Duan for his collaboration in high-fidelity simulation and for his insights into turbulent flow. Sandia National Laboratories is a multi-mission laboratory managed and operated by National Technology and Engineering Solutions of Sandia, LLC., a wholly owned subsidiary of Honeywell International, Inc., for the U.S. Department of Energy's National Nuclear Security Administration under contract DE-NA0003525.

References

[1] Gaurini, S. E., Moser, R. D., Shariff, K., and Wray, A., "Direct numerical simulation of a supersonic turbulent boundary layer at Mach 2.5," *Journal of Fluid Mechanics*, Vol. 414, 2000, p. 1–33. https://doi.org/10.1017/S0022112000008466.

[2] Pirozoli, and Bernadini, "Turbulence in Supersonic Boundary Layers at Moderate Reynolds Numbers," *Journal of Fluid Mechanics*, Vol. 668, 2011, p. 120–168. https://doi.org/10.1017/jfm.2011.368.

[3] Poggie, J., *Compressible Turbulent Boundary Layer Simulations: Resolution Effects and Turbulence Modeling*, 2015. https://doi.org/10.2514/6.2015-1983.

[4] Trettel, A., and Larsson, J., "Mean velocity scaling for compressible wall turbulence with heat transfer," *Physics of Fluids*, Vol. 28, No. 2, 2016, p. 026102. https://doi.org/10.1063/1.4942022.

[5] Huang, J., Zhang, C., Duan, L., and Choudhari, M. M., *Direct Numerical Simulation of Hypersonic Turbulent Boundary Layers inside an Axisymmetric Nozzle*, 2017. https://doi.org/10.2514/6.2017-0067.

[6] GS, S., and Candler, G. V., "Subgrid-scale effects in compressible variable-density decaying turbulence," *Journal of Fluid Mechanics*, Vol. 846, 2018, p. 428–459. https://doi.org/10.1017/jfm.2018.281.

[7] Duan, L., Nicholson, G. L., Huang, J., Casper, K. M., Wagnild, R., and Bitter, N., *Direct Numerical Simulation of Nozzle-Wall Pressure Fluctuations in a Mach 8 Wind Tunnel*, 2019. https://doi.org/10.2514/6.2019-0874.

[8] Huang, J., Nicholson, G. L., Duan, L., Choudhari, M. M., and Bowersox, R. D., *Simulation and Modeling of Cold-Wall Hypersonic Turbulent Boundary Layers on Flat Plate*, 2020. https://doi.org/10.2514/6.2020-0571.

[9] Huang, J., Duan, L., Casper, K. M., Wagnild, R., and Bitter, N., *Direct Numerical Simulation of Turbulent Pressure Fluctuations over a Cone at Mach 8*, 2020. https://doi.org/10.2514/6.2020-1065.

[10] Nicholson, G. L., Huang, J., Duan, L., Choudhari, M. M., Morreale, B., and Bowersox, R. D., *Budgets of Reynolds Stresses and Turbulent Heat Flux for Hypersonic Turbulent Boundary Layers Subject to Pressure Gradients*, 2022. https://doi.org/10.2514/6.2022-1059.

[11] Liu, Y., Schuabb, M., Duan, L., Paredes, P., and Choudhari, M., *Interaction of a Tunnel-like Acoustic Disturbance Field with a Blunt Cone Boundary Layer at Mach 8*, 2022.

[12] Casper, K. M., Beresh, S. J., Wagnild, R., Henfling, J., Spillers, R., and Pruett, B., *Simultaneous Pressure Measurements and High-Speed Schlieren Imaging of Disturbances in a Transitional Hypersonic Boundary Layer*, 2013. https://doi.org/10.2514/6.2013-2739.

[13] Casper, K. M., Beresh, S. J., Henfling, J. F., Spillers, R. W., Pruett, B. O. M., and Schneider, S. P., "Hypersonic Wind-Tunnel Measurements of Boundary-Layer Transition on a Slender Cone," *AIAA Journal*, Vol. 54, No. 4, 2016, pp. 1250–1263. https://doi.org/10.2514/1.J054033.

[14] Smith, J. A., DeChant, L. J., Casper, K. M., Mesh, M., and Field, R. V., *Comparison of a Turbulent Boundary Layer Pressure Fluctuation Model to Hypersonic Cone Measurements*, 2016. https://doi.org/10.2514/6.2016-4047.

[15] Miller, N. E., Lynch, K. P., Gordeyev, S., Guildenbecher, D. R., Duan, L., and Wagnild, R. M., *Aero-Optical Distortions of Turbulent Boundary Layers: Hypersonic DNS*, 2022. https://doi.org/10.2514/6.2022-0056.

[16] Howard, M., Bradley, A., Bova, S. W., Overfelt, J., Wagnild, R., Dinzl, D., Hoemmen, M., and Klinvex, A., *Towards Performance Portability in a Compressible CFD Code*, 2017. https://doi.org/10.2514/6.2017-4407.

[17] Marineau, E. C., Morraru, G. C., and Daniel, D., *Sharp Cone Boundary-Layer Transition and Stability at Mach 14*, ???? https://doi.org/10.2514/6.2017-0766, URL https://arc.aiaa.org/doi/abs/10.2514/6.2017-0766.

[18] Subbareddy, P. K., and Candler, G. V., "A fully discrete, kinetic energy consistent finite-volume scheme for compressible flows," *Journal of Computational Physics*, Vol. 228, No. 5, 2009, pp. 1347–1364. https://doi.org/https://doi.org/10.1016/j.jcp.2008.10.026.

[19] Larsson, J., *Large eddy simulation of the HyShot II scramjet combustor using a supersonic flamelet model*, 2012. https://doi.org/10.2514/6.2012-4261.

[20] Nompelis, I., Drayna, T., and Candler, G., *A Parallel Unstructured Implicit Solver for hypersonic reacting flow simulation*, 2005.

[21] Candler, G. V., Johnson, H. B., Nompelis, I., Subbareddy, P. K., Drayna, T. W., and Gidzak, M. D., V. andBarnhardt, *Development of the US3D Code for Advanced Compressible and Reacting Flow Simulations*, 2015. https://doi.org/10.2514/6.2015-1893.

[22] Allmaras, S. R., Johnson, F. T., , and Spalart, P. R., *Modifications and Clarifications for the Implementation of the Spalart-Allmaras Turbulence Model*, 2012.

[23] Glowacki, W., "NOL Hypervelocity Wind Tunnel Report No. 2: Nozzle Design," , ????

[24] Johnson, H. B., and Candler, G. V., *Hypersonic Boundary Layer Stability Analysis Using PSE-Chem*, 2005.

[25] Balakumar, P., and Chou, A., "Transition Prediction in Hypersonic Boundary Layers Using Receptivity and Freestream Spectra," *AIAA Journal*, Vol. 56, No. 1, 2018, pp. 193–208. https://doi.org/10.2514/1.J056040.

[26] Chaudhry, R. S., and Candler, G. V., *Recovery of Freestream Acoustic Disturbances from Stagnation Pressure Spectrum in Hypersonic Flow*, 2016. https://doi.org/10.2514/6.2016-2059.

[27] Alder, M. C., Gonzalez, D. R., Stack, C. M., and Gaitonde, D. V., "Synthetic generation of equilibrium boundary layer turbulence from modeled statistics," *Computers and Fluids*, Vol. 165, 2018, pp. 127–143.

[28] Corcos, G. M., "The Structure of the Turbulent Pressure Field in Boundary-Layer Flows," *Journal of Fluid Mechanics*, Vol. 18, 1964, pp. 353–378.

[29] Devenport, W. J., and Lowe, K. T., "Equilibrium and non-equilibrium turbulent boundary layers," *Progress in Aerospace Sciences*, Vol. 131, 2022, p. 100807. https://doi.org/https://doi.org/10.1016/j.paerosci.2022.100807, URL https://www.sciencedirect.com/science/article/pii/S0376042122000033.